Eur. Phys. J. B **13**, 661–669 (2000)

THE EUROPEAN PHYSICAL JOURNAL B

EDP Sciences

Study of the symmetry of single-wall nanotubes by electron diffraction

L. Henrard[1,2], A. Loiseau[2,a], C. Journet[1], and P. Bernier[1]

[1] Groupe de Dynamique des Phases Condensées, Université de Montpellier II, Place E. Bataillon CC 026, 34095 Montpellier Cedex 05 France
[2] Laboratoire d'Étude des Microstructures[b], Onera BP 72, 92322 Chatillon Cedex, France

Received 5 February 1999

Abstract. Determining precisely the atomic structure of single-wall carbon nanotubes is essential since it tailors electronic properties of this new carbon material. Here, we present a quantitative electron diffraction study of electric-arc produced single-wall carbon nanotube bundles, combined with simulations based on the kinematic theory and with real-space images. We stress the importance of the twist of the bundle in the interpretation of our data and we analyze both packing lattice parameters and chirality distribution. We show that, within a given bundle, no chirality is favoured whereas SWNT diameters are almost uniform.

PACS. 61.14.-x Electron diffraction and scattering – 61.48.+c Fullerenes and fullerene-related materials – 61.46.+w Clusters, nanoparticles, and nanocrystalline materials

1 Introduction

Since their discovery in 1991 [1], carbon nanotubes (CNs) have been extensively studied both theoretically and experimentally and many possible uses of these molecules have been proposed [2–7]. Within the framework of these studies, single-wall carbon nanotubes (SWNTs) or self-organized ropes of SWNTs have proved to be the best system to investigate the properties of this new material, due to their intrinsic simplicity. Their discovery, [8], has been rapidly followed by their mass production: SWNTs are currently produced using either the laser ablation of carbon rods [9] or the arc-discharge evaporation of graphitic electrodes [10]. Both methods have been shown to lead to the growth of bundles of tens (usually from 20 up to 100) of SWNTs. Many studies have been carried out for discovering and understanding the underlying physics of this new family of carbon compounds. However, the physical properties of these molecules are highly structure - sensitive (see for instance [11]) so that the development of new devices requires, first of all, accurate and reliable characterization methods of the atomic structure of the samples.

Two parameters, at least, are needed to determine the structure of a given SWNT: diameter and helicity. In the first bundle analyses [9,10], using X-Ray Diffraction (XRD) experiments and High Resolution Transmission Electron Microscopy (HRTEM), it has been claimed that SWNTs are packed and form a triangular lattice with a lattice parameter of 1.70 nm. Assuming an intertube distance equal to 0.34 nm, it was concluded that the mean tube diameter is equal to 1.36 nm and that the tubes are the armchair (10,10) tubes. However, further investigations have led to somewhat different conclusions revealing a much more complex reality.

First, careful analyses using methods applicable to macroscopic samples, such as resonant Raman or micro-Raman spectroscopy [12] and diffraction experiments by X-rays and neutrons [13], have shown that the tube diameters and the lattice parameter are polydispersed. Typically, Raman investigations have indicated that diameters vary from 1.1 to 1.5 nm. Second, HRTEM images of individual bundles have revealed that within a bundle NTs display a rather uniform diameter [10,14] but that this diameter varies from 1.44 nm up to 1.74 nm when various parts of the synthesis product are inspected [15]. These observations have been reinforced by recent findings that show the diameter to be dependent on the temperature of the oven for laser produced tubes [16,17], and on the gathering position for arc-discharged produced tubes [15,18]. Both local (TEM) and global (Raman, XRD, Neutron) probe investigations can then be reconciled if we assume that individual bundles are formed by NTs of uniform diameter but that this diameter depends on the precise growth conditions and can consequently vary within one sample depending on the growth localisation. Global probes then analyze polydispersed samples.

The helicity of SWNTs has been studied using two kinds of local probe techniques: atomically resolved Scanning Tunneling Microscopy (STM) and Electron Diffraction (ED). The measurements performed using

[a] e-mail: loiseau@onera.fr
[b] UMR 104 ONERA-CNRS

the first technique combined with Scanning Tunneling Spectroscopy (STS) [11,19] have shown that a large variety of chirality and conductivity behaviours are present in laser produced SWNTs. Let us mention that the exact interpretation of these images is not straightforward since the relative contributions of the intrinsic chirality and of the SWNT twist are not solved [20] and that imaging a cylinder with a STM involves non-trivial geometrical distorsions [21]. Moreover, the small number of investigated tubes does not permit reliable statistics of the chirality distribution.

Electron Diffraction (ED) is a very powerful and reliable technique providing a direct determination of the chirality [22]. It has been indeed successfully and unambiguously used for studying the chirality of multi-wall nanotubes (MWNTs) [23–27]. Although the low diffraction power of SWNTs has curbed the analysis of isolated NTs, the packing of tens of SWNTs in bundles avoids this difficulty. Using nano-diffraction, Cowley *et al.* [28] have concluded that most of the tubes obtained by laser ablation are (10,10) non-chiral NTs and that (11,9) and (12,8) tubes are also present. Selected Area Electron Diffraction (SAED) has been performed by Qin *et al.* [29] and Bernaerts *et al.* [30] on the same kind of samples. They have obtained very similar experimental results but have concluded differently. Qin *et al.* have claimed that tubes forming bundles display a quite uniform distribution of helicities whereas Bernaerts *et al.* have concluded in a small dispersion around armchair NTs.

In this article, we present a quantitative SAED analysis of the structure of SWNTs bundles combined with analyses of HRTEM images, for measuring both the diameter and the chirality of the SWNTs. Bundles studied here have been produced by the arc technique described in reference [10]. SAED patterns have been recorded on imaging plates (IPs). This technique has allowed us to obtain a quantitative analysis of the electron current density of the SAED patterns. Our results are discussed with the benefit of simulations based on the kinematical theory of diffraction (presented in Sect. 2). The experimental procedure is described in Section 3, and Section 4 is devoted to the analysis and to the discussion of the results where we conclude that the arc technique seems to lead to a diameter selection but not to any chirality selection.

2 Theory and simulation

2.1 Definitions and theory

SWNTs are commonly referred to by two integers (n,m) that define a vector $\mathbf{c}_{n,m} = n\,\mathbf{a} + m\,\mathbf{b}$ in a 2D hexagonal graphite sheet ($\mathbf{a}$ and $\mathbf{b}$ are unit vectors of the planar network). The NT is built up by rolling the hexagonal sheet around an axis perpendicular to $\mathbf{c}_{n,m}$ (defined as the oz axis throughout this paper). The radius r and the chiral angle θ of the SWNT can be found from

$$r = a/2\pi(n^2 + m^2 + nm)^{1/2}$$
$$\sin\theta = 3m/2\ (n^2 + m^2 + nm)^{-1/2}$$

where $a = |\mathbf{a}| = |\mathbf{b}|$. The (n,n) ($\theta = 30°$) and $(n,0)$ ($\theta = 0°$) cases define non-chiral tubes and are referred as to armchair and zigzag configurations respectively, whereas the (n,m) cases, where $n \neq m$, correspond to chiral tubes. A bundle of NTs is a close-packed triangular arrangement of SWNTs. The associated lattice parameter is $d = (2r + d_t)$ where d_t is the nearest neighbour carbon-carbon distance between atoms belonging to adjacent tubes.

The simulations that we have performed were based on the kinematical diffraction theory of a plane wave by CNs developed by the Namur group [26,31]. Since carbon has only a low diffraction power, the very small thickness of the sample allows the first Born approximation to be satisfactorily used and the total diffraction amplitude $S(\mathbf{k})$ is given by

$$S(\mathbf{k}) = f(k) \sum_j \mathrm{e}^{\mathrm{i}\mathbf{k}\cdot\mathbf{r}_j} \tag{1}$$

where $\mathbf{k}(\mathbf{k}_\perp, k_z)$ is the wave vector transfer, $\mathbf{k}_\perp$ and k_z are the components perpendicular and parallel to the tube axis, respectively, $f(k)$ the atomic form factor and the sum runs over the atomic coordinates. The intensity of the diffracted electron beam is the square modulus of $S(\mathbf{k})$.

After cumbersome analytical work using the helicoidal symmetry of a (l,m) ($l > 0, -l/2 \leq m \leq l$) nanotube and the fact that a tube can be viewed as composed of l (if $m > 0$) or $l - m$ (if $m < 0$) pairs of carbon helices, $S(\mathbf{k})$ writes [26,31]

$$S(\mathbf{k}) = f(k) \sum_l S_l(\mathbf{k}) \delta(k_z - 2\pi l/T) \tag{2}$$

where T is the period of the helix and $S_l(\mathbf{k})$ is basically a sum of Bessel functions related to the honeycomb lattice and to the finite size of the nanotubes in the xoy plane.

We also mention that powder diffraction spectra $I(k)$ (obtained from XRD or neutron experiments) are calculated by averaging the diffracted intensity on a sphere in the reciprocal space, *i.e.*

$$I(k) \sim \iint |S(\mathbf{k})|^2 \,\mathrm{d}^2k/2\pi k^2. \tag{3}$$

2.2 Isolated SWNT

Figure 1 represents the geometry of an ED experiment. The electron beam (supposed to be in the xoz plane) and the tube axis (along oz axis) form an angle φ and the diffraction pattern lies in a plane perpendicular to the electron beam. The oy axis is chosen perpendicular to both the electron beam and the tube axis. The basis vectors in the diffraction plane can be chosen as k_y and k'_z where k'_z is perpendicular to both the electron beam and k_y. Consequently, $k'_z = k_z$ when $\varphi = 90°$. In the previous section (Eq. (2)), we have defined intensity planes in the reciprocal space. The directions of non-zero intensity will then be obtained by intersecting those planes with the Ewald sphere of radius $2\pi/\lambda_\mathrm{e}$, where λ_e is the electron

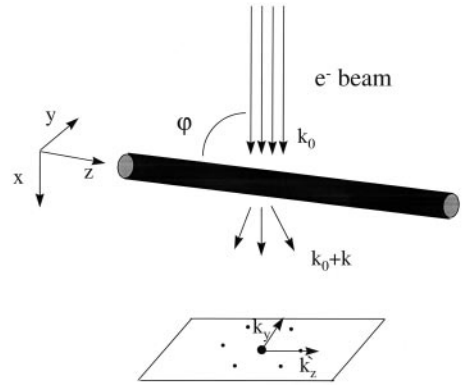

Fig. 1. Schematic representation of the electron diffraction geometry.

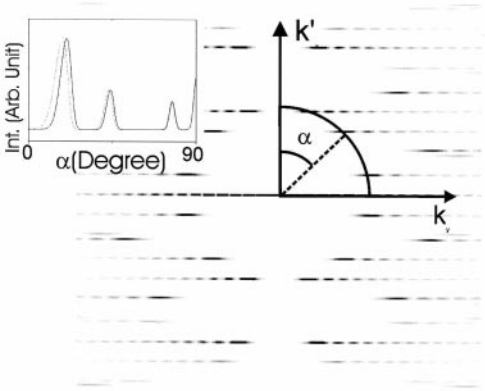

Fig. 2. Simulated diffraction pattern of a (14,6) tubule based on the kinematic theory. The α angle and shell used for the circular profile are defined. Inset: corresponding circular profiles for $\varphi = 90°$ (solid) and $\varphi = 80°$ (dashed).

wavelength. Thanks to the small diffraction angles considered, the resulting circles yield lines of intensity in the diffraction plane marked by $k_z = 2\pi l/T$ where T is the periodicity along oz and l is an integer. They are called layerlines in [26,31].

The intensity along layerlines results from the tubular atomic structure. For example, diffraction patterns related to non chiral tubes present main spots forming an hexagon on concentric circles (hereafter, called first and second circles for the first two). Those circles are defined by a transfer momentum k_1 ($k_1 = 2\pi/d_1$ with $d_1 = 3d_{c-c}/2$ and $d_{c-c} = 1.42$ Å is the carbon-carbon distance) and k_2 ($k_2 = 2\pi/d_2$ and $d_2 = \sqrt{3}d_{c-c}/2$). They are related to the $(1\bar{1}00)$ and $(11\bar{2}0)$ reflections of graphite, respectively. For chiral tubes of chiral angle θ, the 2θ misorientation of the hexagons belonging to the front side and back side of the tubes leads to a pattern presenting two hexagons rotated by 2θ on each circle (see Fig. 2 for an example).

From Figure 2, we also see that spots are elongated perpendicular to k'_z. This phenomenon is called chirping in [26] and is related to (i) the decrease of the lattice parameter seen by the electrons from the center towards the edges of the NTs, as a consequence of the curvature and (ii) to the finite lateral size of the NT. The effect (i) does not affect spots related to C-C bonds parallel to the tube axis and is very important for spots related to C-C bonds perpendicular to the tube axis.

The relative positions of the spots on the first or second circle provide a direct determination of the tube chirality and this property has been already used for the analysis of MWNTs chiralities [23,24,26,27]. The analysis of SWNTs is more difficult due to the low and diffuse intensity of the spots. A convenient way to localise intensity maxima on the first circle is to consider circular profiles, defined as a function of the angular position α (Fig. 2). In order to enhance the signal to noise ratio of the circular profiles, we have integrated the intensity (as a function of the angle α) on circular shells. Providing that the angular interval of investigation and the width of the shell are carefully chosen, one obtains a tractable circular profile, as shown in the inset of Figure 2 for a (14,6) tube. As a consequence of this procedure, circular profiles show peaks (see inset of Fig. 2) instead of delta functions as it should have been for a "perfect" circular profile describing a diffraction pattern made of layerlines. We have studied the effect of the shell width on the positions of the peaks and on their intensity. A too large width leads to a double (or multiple) peak structure for each layerline and makes the interpretation of the circular profile difficult. We have determined that a convenient width value is $0.1k_1$, which insures that the positions of the peaks are not affected by the averaging operation and that they can be correctly related to the chirality angle. Furthermore, as shown in Figure 2, the profile reproduces faithfully the impact of the chirping effect (point (i) in the previous paragraph), on the intensity of the peaks which decreases for increasing α as expected theoretically.

Until now, the description of the diffraction patterns was restricted to nanotubes strictly perpendicular to the electron beam ($\varphi = 90°$ in Fig. 1). A misorientation ($\varphi \neq 90°$) leads to a change of symmetry of the projected tube. As a consequence, the projected period along z' increases and the layerlines move to higher k'_z [23]. From geometrical considerations, it is obvious that the layerlines related to higher k'_z are more affected and that the $k'_z = 0$ line does not change as can be seen in the inset of Figure 2 (dashed line).

2.3 Bundles of SWNTs

Diffraction patterns of a bundle of SWNTs are also obtained from equation (1) where the sum then runs on all the helices of all the tubes packed into a triangular lattice of parameter d. No orientation relationship or position correlation between adjacent tubes has been assumed in the calculations.

Figure 3 (upper part) shows the diffraction pattern calculated for a bundle composed of 55 tubes such as $r = 6.8$ Å $\pm\, 0.1$ Å and corresponding to 8 different helicities ((10,10) ($r = 6.78$ Å, $\theta = 30°$), (11,9) ($r = 6.79$ Å, $\theta = 27°$), (12,8) ($r = 6.82$ Å, $\theta = 23°$), (13,7) ($r = 6.88$ Å, $\theta = 20°$), (14,5) ($r = 6.67$ Å, $\theta = 15°$), (15,4) ($r = 6.79$ Å,

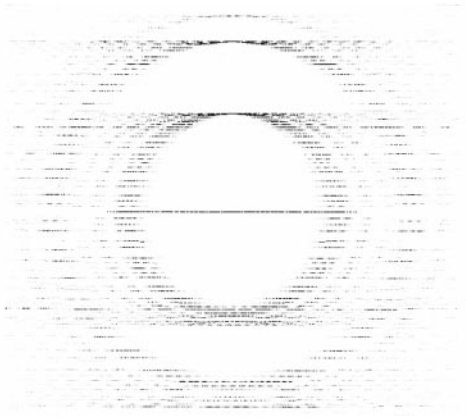

Fig. 3. Simulated diffraction pattern of a bundle of 55 tubes. A triangular lattice with $d = 16.8$ Å is assumed. The bundle is formed from a random distribution of (10,10), (11,9), (12,8), (13,7), (14,5), (15,4), (16,2) and (17,0) tubes. The upper part is for $\phi = 90°$ and the lower part is for $\phi = 60°$.

$\theta = 12°$), (16,2) ($r = 6.68$ Å, $\theta = 6°$), (17,0) ($r = 6.85$ Å, $\theta = 0°$)) and packed into a triangular lattice with $d = 16.8$ Å. Two rings of intensity, associated with the first and second diffraction circles can be distinguished. The layerlines associated with the different helicities are clearly visible. As a consequence of the chirping effect discussed in Section 2.2, the diffraction pattern of a bundle made of NTs of random chiralities shows a well defined intensity close to $\alpha = 0°$ and more diffuse spots close to $\alpha = 90°$. Also notice that the second ring displays the same general features as the first one.

Finally the effect of a misorientation of the bundle with respect to the electron beam is shown in Figure 3 (lower part) where the incident angle $\varphi = 60°$ instead of $\varphi = 90°$. As mentioned in Section 2.2, the main influence of the tube misorientation is to increase the k'_z value for each layerline. The result is that a large composite band appears close to $\alpha = 0°$. This band is therefore the signature of the existence of a chirality distribution within the bundle.

2.4 $k_z = 0$ line

The central line ($k'_z = 0$) of diffraction patterns has a particular interest when studying bundles of SWNTs as being a fingerprint of the packing of the tubes along the y direction. An example is shown in Figure 4 for the bundle of 55 nanotubes previously described and oriented with the [10] axis of the triangular lattice along the y direction (solid curve (a)). The peaks are the (h0) reflections of the packing lattice and their spacing provides a direct determination of the lattice parameter.

Calculations have been also done in a continuum approximation (dashed lines) using the following density

$$\sigma(\mathbf{r}) = \sum_i \delta(|\mathbf{r} - \mathbf{R}_i| - \rho_i) \tag{4}$$

where the sum runs over all the tubes (labelled by i), $\mathbf{R}_i$ and ρ_i are the position of the tube center in the xoy plane

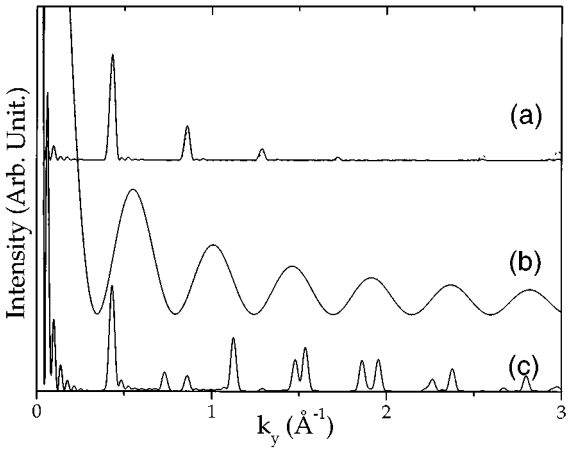

Fig. 4. Simulated central line profile of an electron diffraction pattern ($\varphi = 90°$) for the 55 tubes bundle (same as in Fig. 3) (curve (a)) and for an isolated (14,6) tube (curve (b)). The solid curves correspond to the kinematic atomistic theory and the dashed lines (undistinguishable in curves (a) and (b)) to the continuum approximation. Curve (c) is an average spectrum over all 2D triangular crystal orientations (powder diffraction-like spectra) in the continuum theory.

and the radius of the tube i, respectively. Using

$$S(\mathbf{k}) = f(k) \iiint \sigma(\mathbf{r}) \mathrm{e}^{\mathrm{i}\mathbf{k}\cdot\mathbf{r}} \mathrm{d}^3 r \tag{5}$$

one obtains

$$S(\mathbf{k}) = 2\pi\delta(k_z) f(k) \sum_i \rho_i J_0(\mathbf{k}_\perp \rho_i) \mathrm{e}^{-\mathrm{i}\mathbf{k}_\perp \cdot \mathbf{R}_i} \tag{6}$$

where J_0 is the Bessel function of order 0. Figure 4 allows one to compare continuum (dashed lines in Fig. 4) and atomistic (solid lines) calculations for both the packing of tubes (curve (a)) and a single (14,6) nanotube (curve (b)). Curve (b) corresponds to the well-known form factor of one carbon nanotube. It is clear from this comparison that the exact atomic structure is not important for low k_y transfer in the central line ($k'_z = 0$) and that the intensity variations in this region ($k_y < 2$ Å^{-1}) of the diffraction space are only related to the packing of what can be considered as dense carbon cylinders.

Finally, we mention that the neutron diffraction or XRD of powders of SWNTs bundles results from the averaging of $S(\mathbf{k})$ over all directions [13]. For $k_y < k_1$ (see Sect. 2.2 for definition), this is also similar to average diffraction intensities over all the orientations of the triangular lattice with respect to the electron beam. In particular, the central line of the ED pattern is similar to a neutron diffraction spectrum if the bundle freely rotates around the z axis and if we neglect the variation of the form factor. Curve (c) of Figure 4 gives the profile resulting from such a rotational average. This point will be useful for the analysis of some features of the experimental ED patterns.

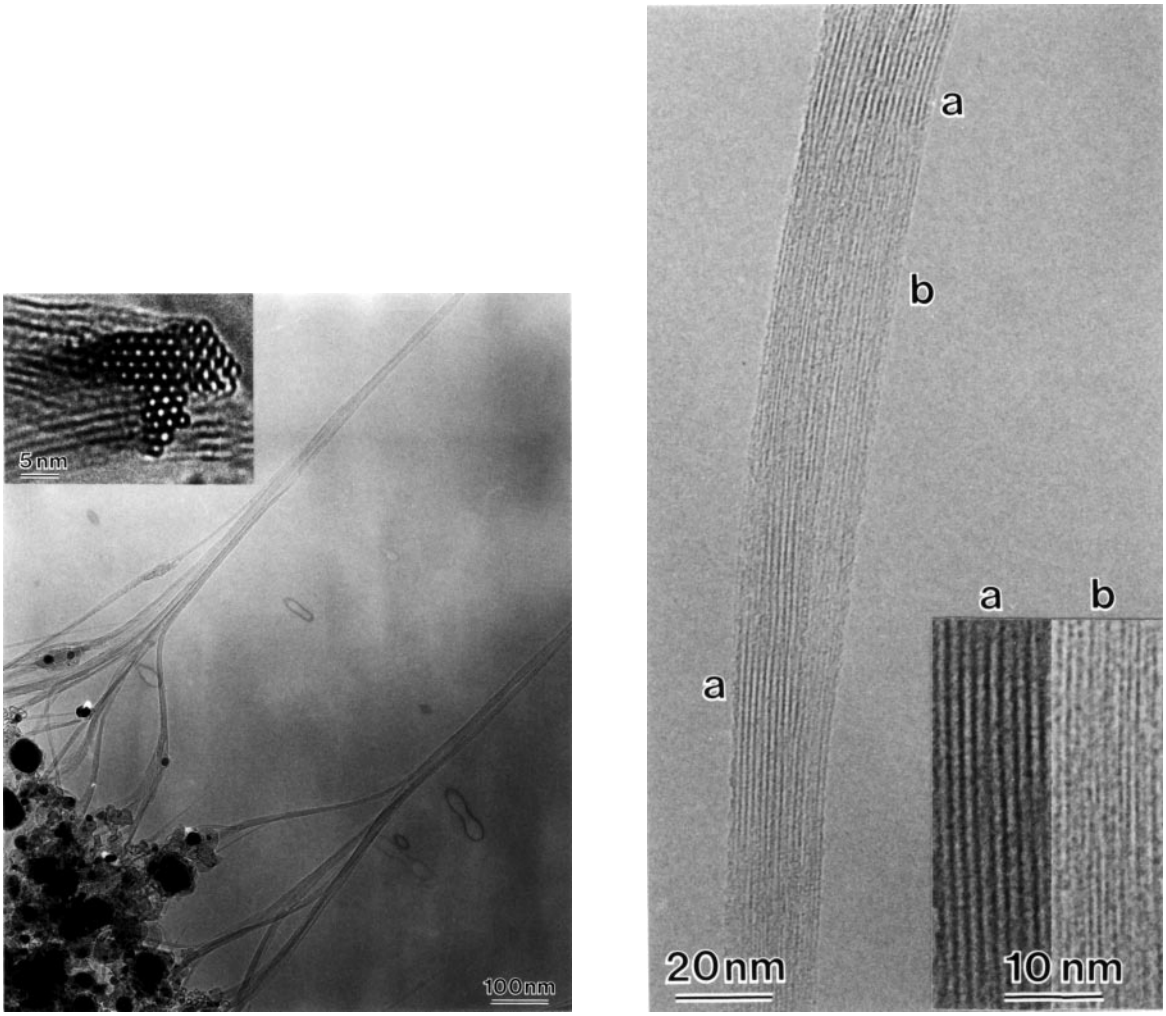

(a) (b)

Fig. 5. HRTEM images of bundles produced by the arc technique. (a) General view of isolated large bundles resulting from a branching of various smaller bundles. Inset: cross-section like view of a polycrystalline bundle. (b) View of a twisted bundle with its axis normal to the electron beam. The tube packing is imaged as a set of diffraction fringes related to lattice planes in Bragg conditions. The interfringe distance depends on the orientation of the triangular lattice with respect to the electron beam. Due to the twist of the bundle, the fringe spacing varies along the tube axis according to a definite sequence. The inset shows a magnification of fringes related to (11) and (10) lattice planes.

3 Experimental procedure

Bundles of SWNTs were produced by the arc-discharge between electrodes composed of carbon and catalysts (Ni,Y) in a He atmosphere (660 mbar) as described in [10]. The material produced mainly consisted of a collaret formed on the cathode. We collected a small fraction in the best part of this collaret, that is the part which contained the largest bundles [15]. This material was then dispersed ultrasonically into an ethanol bath and then transferred mechanically to a TEM grid. High resolution (HR)-TEM images and diffraction patterns were obtained on a JEOL 4000 FX microscope working at 400 keV. Isolated straight bundles of SWNTs (see the example in Fig. 5) have been carefully selected for recording the SAED. An important technical point of the procedure was that the SAED patterns were recorded on imaging plates (IPs) developed by Fuji instead of the usual films. Thanks to this technique, we have obtained a linear relationship, over 14 orders of magnitude, between the diffracted electron density and the levels read after developing the IPs. A typical exposure time of the IPs was 90 seconds and the beam was defocussed in order to have well defined spots. Care was also taken in controlling the stability of the system during the acquisition of the SAED patterns.

Figure 6 shows a typical ED pattern that we obtained on an isolated straight bundle of SWNTs. More than ten similar images have been recorded. The main features are a line of intensity crossing the central spot (called central line hereafter) and two circles of quasi continuous intensity. We note that the central line is spotty and that

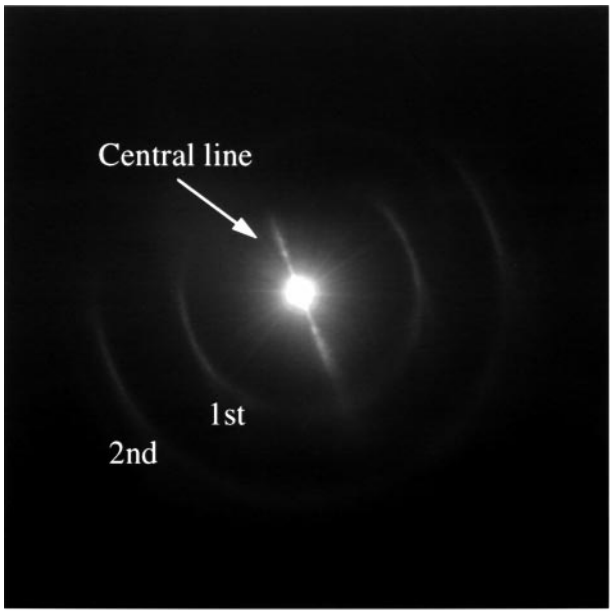

Fig. 6. Experimental diffraction pattern of an isolated straight SWNTs bundle.

the intensity along the circles is not uniform even if no well defined spots can be observed. In the next section, we will relate these features to the nature of the tube packing and to the chirality distribution.

4 Results and discussions

4.1 TEM images

Bundles are characterized by two main features which are emphasized in the examples displayed in Figures 5a and 5b. First, bundles involving more than 20 or 30 SWNTs most often result from a branching process of several bundles (a typical example is shown in Fig. 5a). This branching is most probably due to a van der Waals attraction between individual bundles. As a consequence, most of the bundles we have analysed are made up of several two dimensional SWNTs crystals differently oriented. The inset in Figure 5a shows a cross-section-like view of such a polycrystalline bundle oriented with its axis along the beam direction. In such images, individual tubes are seen as white dots located at tube centers so that the various 2D triangular lattices are clearly visible.

The second feature we want to draw attention to is exemplified in Figure 5b. The bundle, lying perpendicular to the electron beam, is imaged as a set of fringes corresponding to the lattice planes of the tube packing in Bragg orientation as widely reported [9,10,15]. However one sees that the fringe periodicity varies along the bundle axis and the inset shows the fringe sets relative to (10) and (11) lattice planes which are rotated from each other by 30°. We therefore attribute this observation to a twist of the whole bundle and consequently to the fact that various orientations of the NTs crystal face the electron beam. The mean period of the twist is found to be frequently associated with a twist angle of 1°/nm even if large variations are found. This rather irregular twist is not unexpected regarding the complicated mesh of bundles and catalyst particles that is obtained from the plasma, the subsequent sonication and the mechanical transfer to the TEM grid. All these steps lead to mechanical stress on bundles that are, furthermore, easy to twist.

Consequences of these observations on the diffraction patterns will be drawn in the next sections.

4.2 Central $k_z = 0$ line

Let us first notice that the central line is actually a double triangle pointing on the central spot. The opening angle is obviously the direct consequence of the fact that the 2D SWNTs crystal axis is not straight along all the selected area. Three reasons can be put forward: i) The bundles are not straight but curved. Even if we have selected the most straight bundles, a curvature of a few degrees could not be ruled out. ii) Vibration of the bundle. We take care to minimize this effect by choosing bundles fixed (or lifted on the carbon membrane) at both ends. iii) The already mentioned twist of bundles. This twist is such that the "2D crystal orientation" precesses around the bundle direction.

The value of the triangle opening is then a measurement of the maximum of the disorientation of the "2D crystal orientation" and gives a maximum value ($\beta_{\max}$) for the twist. From our recorded spectra, we have found a mean value lying around $\beta_{\max} = 5°$. This number is consistent with the twist angle measured in HRTEM images.

We now turn to the profile of the central line. Figure 7 (upper curves a–e) shows examples of profiles obtained from our diffraction patterns. We first note that they are very similar and display all main peaks around 1 Å^{-1} and 1.4 Å^{-1}. Some less reproducible structures are found around 0.5 Å^{-1} on curve (d) and around 0.8 Å^{-1} on curve (a). We also note that peaks in curves (b) and (e) lie at slightly higher momentum transfer.

Here, let us remind that according to Section 2.4, the peak positions on the central line depend on the orientation of the 2D SWNTs crystal with respect to the electron beam. Considering that all profiles are similar and that we could not reasonably claim that all the observed bundles present the same orientation with respect to the electron beam, we conclude that the observed profiles correspond to an average over many crystal orientations. These average spectra can come both from the presence of various 2D microcrystals of NTs and from the twist mentioned before.

Comparison with calculation gives even more insights in the SWNTs bundle structure. We have compared experimental spectra with calculations made for a random orientation of the bundle as described by equation (6). The results are displayed at the bottom (curves (f)) of Figure 7. The left part of the figure comes from equation (6) and the right part is the result of a Gaussian convolution of the original spectra in order to simulate effects of the aperture

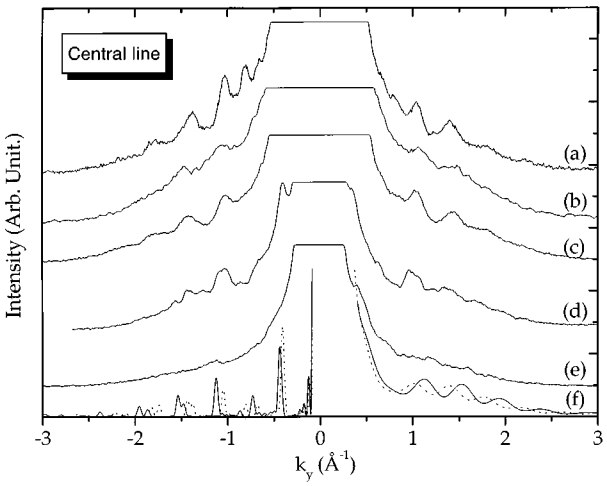

Fig. 7. Central line profiles of different ED patterns. Curves (a–e) are experimental results. Curves (f) show the diffraction patterns for two different bundles calculated within the continuum approximation. The left part of curves (f) ($k_y < 0$) directly result from equation (6) and in the right part ($k_y > 0$), spectra have been convoluted with a Gaussian function. The solid and dashed lines are for $d = 16.8$ Å ($r = 6.8$ Å and $d_t = 3.2$ Å) and for $d = 18.2$ Å ($r = 7.5$ Å and $d_t = 3.2$ Å), respectively.

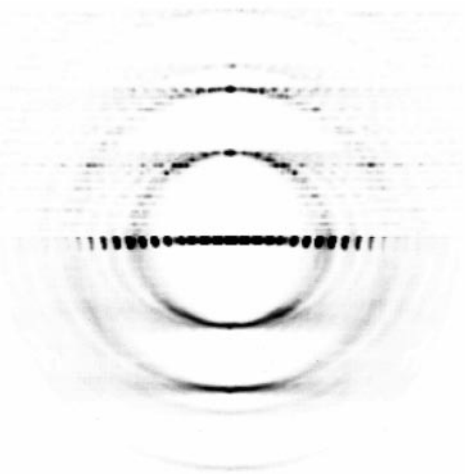

Fig. 8. Simulated electron diffraction pattern. Upper part: same as Figure 4 but with a gaussian convolution. Lower part: a misorientation ($\beta_{\max} = 5°$) average has been performed in order to simulate the twist of the bundle.

used experimentally. Spectra are shown for two kinds of bundles: solid and dashed curves are for a SWNTs triangular lattice of parameter $d = 16.8$ Å ($r = 6.8$ Å, $d_t = 3.2$ Å) and $d = 18.2$ Å ($r = 7.5$ Å, $d_t = 3.2$ Å) respectively.

By comparing the simulated curves and experimental spectra, it comes out that experimental curves (a), (c) and (d) are in good agreement with simulations done with $r = 7.5$ Å and that smaller tubes ($r = 6.8$ Å) are necessary for fitting curves (b) and (e). Furthermore, from the peak width and the level of the background, we estimate that the values of r are determined with a precision of roughly ± 0.2 Å. These values are consistent with the fringe spacings measured in HRTEM images and with the analysis of the tube diameters on section-like view images [15]. The diameter range and polydispersity which can be deduced from these results are consistent with neutron diffraction [13], XRD [9,10] and Raman spectroscopy [12] data. Let us also note that (i) since we have studied individual bundles collected from a small fraction of the produced material, the results are not a mean value over the whole sample as it is with global probe experiments. (ii) The deduced value of r depends also on the value assumed for d_t as in all diffraction experiments done on SWNTs bundles.

We then conclude that the central line provides quantitative information on the lattice parameters of the triangular arrangement of SWNTs within bundles. We have found 6.8 Å $< r < 7.5$ Å which is consistent with the value obtained by inspection of HRTEM images [15]. We have also shown that, over the selected area of the bundle, a crystal orientation average takes place. We have attributed this phenomenon to both a polycrystalline order in the bundle and a twist of the whole bundle in consistence with HRTEM images.

4.3 Intensity along the first circle

We now turn to the inspection of the main features of the diffraction patterns, *i.e.* the intensity along the first circle. We have already mentioned (Sect. 3) that these circles are neither uniformly intense, nor clearly spotty. Here we discuss this observation in more detail.

First of all, in agreement with the calculations, intensity is more important close to $\alpha = 0°$ and becomes more and more diffuse and weak as α increases. It is lost in the background for α close to $90°$. However, direct comparison between Figures 3 and 6 is not directly meaningful. In Figure 8 (upper part), we present a simulation of the ED pattern of the 55 tubes bundle described in Section 2.3 where we have convoluted each spot by a Gaussian in order to simulate the experimental broadening due to the finite size of the aperture and to the divergence of the electron beam. A close inspection of Figure 8 (upper part) reveals that the intensity along the circles is a little bit spotty which is in contrast to what is observed in experimental patterns. Two reasons can be put forward. (i) The analysed bundle involves more different chiralities than those used in the simulations. (ii) A geometrical effect, such as the twist of the bundle, wash out these spots.

Concerning the first effect, it is obvious that broadening the chirality distribution in the simulations gives rise to a more continuous intensity profile. This implies to release the constraint on the tube diameters which was fixed to 0.1 Å in the simulations. Experimentally, we have estimated in the previous section that the dispersion in the diameters is about ± 0.2 Å. Such a dispersion associated to a random chirality distribution will lead to an almost continuous profile as experimentally observed.

The second effect we want to explore is the geometrical twist of the bundle, which is very frequently observed. The main effect of this twist is that the NTs axes are locally precessing around the bundle axis. This precession can be decomposed into two rotation operations. For the first operation, we assume $\varphi = 90°$ and we consider a rotation of the tube axis around ox, that is around the electron beam (Fig. 1): this leads to a simple rotation of the diffraction pattern in the diffraction plane. The second operation consists of rotating the tube axis around oy ($\varphi \neq 90°$): the effect is to move the diffraction spots along the first circle towards larger α (larger k'_z). We have then modelled the effect of the twist by an average on the two misorientation directions described above and for a twist angle $\|\beta\| < \beta_{\max}$, where $\beta_{\max}$ is related to the twist periodicity. As already mentioned, $\beta_{\max}$ can be measured from the opening of the central line. We have obtained a realistic value of $\beta_{\max} = 5°$. Figure 8 (lower part) shows the result of this twist effect. The spotty character of the first circle has now disappeared and comparison with Figure 6 is very satisfactory. Moreover, as discussed in Section 4.2, the twist induces a triangular opening of the k'_z line which reproduces the experimental observations very well.

It is worth mentioning that in reference [30], the authors have also analysed the impact of the bundle twist on the diffraction patterns in terms of misorientation. However this analysis was restricted to the effect of a simple rotation of the bundle around a single axis, whereas here the twist is modelled as a complete precession of the bundle crystal around the bundle axis. Moreover, the above authors did not consider any dispersion of both the chirality and the diameter nor its coupling with the twist effect.

An even more quantitative description of intensity variations along the intensity circle is provided by the circular profile processed according to the procedure defined in Section 2.2. The experimental data have been treated using the Semper package and the shell width of averaging has been chosen to be $0.1k_1$. Figure 9 shows three experimental profiles (a–c) and the profile calculated for a straight bundle ($\varphi = 90°$ (d) and for the twisted bundle ($\beta_{\max} = 5°$ (e), same bundle as in Fig. 8 upper part). The general agreement between experiments and simulations has again to be emphasized. Moreover, the experimental spectra (a) and (b) display several peaks. First, we can rule out a noisy origin of these peaks because of the symmetry of their positions around $\alpha = 0$ and because they also appear symmetrically around $\alpha = 180°$ (not shown). Moreover for a chiral tube, a peak at angle α should be associated to a peak at $\alpha' = 60° - \alpha$ (see Fig. 2). These peaks are also seen in spectra (a) and (b) even if they are hardly visible due to the background. These peaks can therefore be related to an excess of tubes with a given chirality. For example peaks at $5°, 12°$ and $22°$ are seen in spectrum (b) and peaks at $15°$ and $18°$ in spectrum (a). These peak positions are directly associated with chiral angles θ and can be related to different tube configurations using the simulations. For example, peaks at $5°$ could come from a $(17, 2)$ tube ($r = 7.07$ Å, $\theta = 5.5°$), peaks at $12°$ from a $(15, 4)$ tube ($r = 6.79$ Å, $\theta = 11.5°$), the peaks at $22°$ from $(12, 8)$ tube ($r = 6.82$ Å, $\theta = 23.4°$).

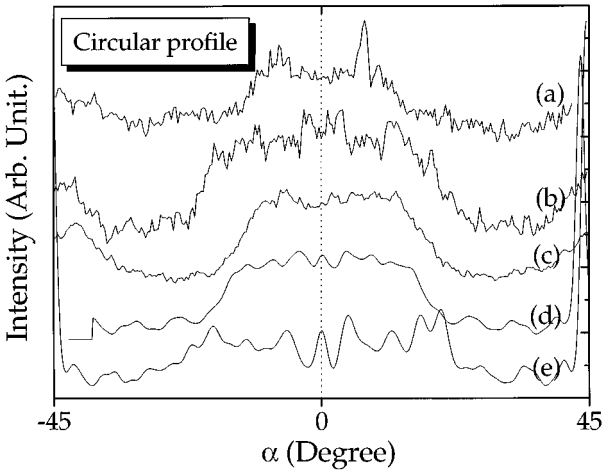

Fig. 9. Circular profiles extracted from three experimental diffraction patterns (a–c). Curves d and e are calculated circular profiles for a 55 tubes bundle with (d) and without (e) simulation of a twist.

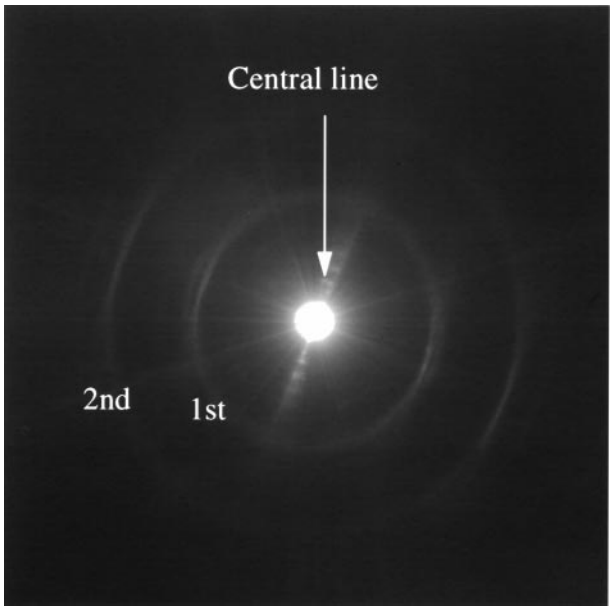

Fig. 10. Experimental diffraction pattern of an isolated straight SWNT bundle, probably misoriented with respect to the electron beam.

Finally, in Figure 10, we display another experimental diffraction pattern we have obtained several times. The main difference with Figure 6 is a doubling of the diffraction arcs. Figure 11 shows a diffraction pattern calculated for the 55 tube bundle used before but tilted by an angle $\varphi = 60°$. The same convolution and twist average procedures as those used for Figure 8 were performed. This simulated diffraction reproduces the double circle pattern that we have found in experimental ED. As discussed in Section 2.3 this is another proof that bundles are composed of tubes with random chirality.

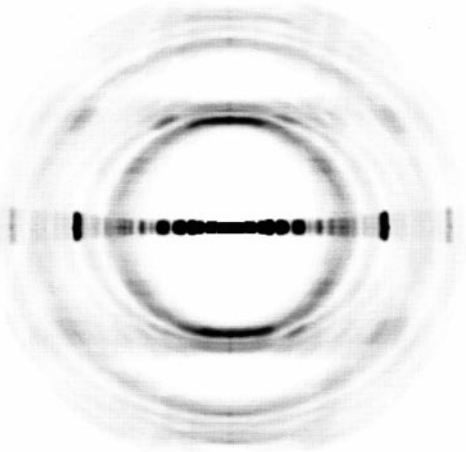

Fig. 11. Same as Figure 8 with $\varphi = 60°$.

5 Conclusion

In this study, we have performed a combined HRTEM and ED analysis of bundles of SWNTs produced by the arc-discharge technique. The use of both imaging plate recording facilities and quantitative simulation permits us to have a deeper insight into the analysis of the diameter of the tubes and the chirality distribution of SWNTs forming bundles. The best fit of the experimental ED patterns on individual bundles has been obtained for a packing of tubes of uniform diameter but with random chirality.

Our conclusions are in good general agreement with STM analysis, optical data or Raman spectroscopy. The diameter polydispersity found here is slightly smaller than that obtained from X-ray or Raman studies, simply because of the sampling chosen for our analyses. Results on chirality nicely confirm STM observations. They are however in contradiction with the previous ED studies of bundles of SWNT presented in [28,30] but are in agreement with the conclusions of [29]. We have no definitive explanation for this disagreement. Some discrepancies could be due to different experimental conditions (electron irradiation damaging, ...). However, we emphasize that the results [28,30] were obtained on laser produced SWNTs and that, to the best of our knowledge, no definitive conclusion on the similarities or differences of laser or arc-discharge samples can be made. In particular a recent comparison of arc discharge and laser bundles using Raman spectroscopy has revealed that the diameter dispersions are different in both kinds of samples [32]. One can also infer that the chirality distribution could be different. However our results are nicely consistent with very recent detailed EELS studies of laser produced SWNTs bundles [33]. We intend to apply, in the near future, our method of characterization to the study of laser produced SWNTs in order to clarify this point.

It is a great pleasure to thank N. Demoncy and M. Hÿtch for help in the use of imaging plates and for useful discussions about the present results. A. Lucas and Ph. Lambin who provided us with the Fortran code used in reference [31] are gratefully acknowledged for their continuous interest in this work. One of us (LH) is supported by the TMR European network NAMITECH (ERBFMRX-CT96-0067 (DG12 - MIHT)).

References

1. S. Iijima, Nature **354**, 56 (1991).
2. M.M.J. Treacy, T.W. Ebbesen, J.M. Gibson, Nature **381**, 678 (1996); J.L. Liu, Phys. Rev. Lett. **79**, 1297 (1997); E. Hernandez, C. Goze, P. Bernier, A. Rubio, Phys. Rev. Lett. **80**, 4502 (1998).
3. P.G. Collins *et al.*, Science **278**, 100 (1997); S.J. Tans, A.R.M. Verschueren, C. Dekker, Nature **393**, 49 (1998).
4. Y. Saito, Appl. Phys. A **67**, 95 (1998); W.A. de Heer, A. Chatelain, D. Ugarte, Science **270**, 1179 (1995).
5. H. Dai *et al.*, Nature **384**, 147 (1996).
6. A.C. Dillon *et al.*, Nature **386**, 377 (1997).
7. S. Frank *et al.*, Science **280**, 1744 (1998).
8. D.S. Bethune *et al.*, Nature **363**, 605 (1993).
9. A. Thess *et al.*, Science **273**, 483 (1996).
10. C. Journet *et al.*, Nature **388**, 756 (1997).
11. J.W.G. Wildoer *et al.*, Nature **391**, 59 (1998).
12. P.C. Eklund, J.M. Holden, R.A. Jishi, Carbon **33**, 959 (1995); M. Lamy de la Chapelle *et al.*, Carbon **36**, 705 (1998); E. Anglaret *et al.*, Carbon (in press).
13. S. Rols *et al.*, Eur. Phys. J. B **10**, 263 (1999).
14. C. Journet, P. Bernier, Appl. Phys. A **67**, 1 (1998).
15. C. Journet, Ph.D. thesis, University of Montpellier, 1998.
16. S. Bandow *et al.*, Phys. Rev. Lett. **80**, 5003 (1998).
17. A.G. Rinzler *et al.*, Appl. Phys. A **67**, 29 (1998).
18. M. Lamy de la Chapelle *et al.* (unpublished).
19. T.W. Odom *et al.*, Nature **391**, 62 (1998).
20. W. Clauss, D.J. Bergeron, A.T. Johnson, Phys. Rev. B **58**, R4266 (1998).
21. V. Meunier, Ph. Lambin, Phys. Rev. Lett **81**, 5588 (1998).
22. L.C. Qin, Chem. Phys. Lett. **297**, 23 (1999).
23. X.P. Zhang, X.B. Zhang, G. Van Tendeloo, S. Amelinckx, M. Op de Beeck, J. Van Landuyt, J. Cryst. Growth **130**, 368 (1993).
24. X.B. Zhang, X.P. Zhang, S. Amelinckx, G. Van Tendeloo, J. Van Landuyt, Ultramicroscopy **54**, 237 (1993).
25. M. Liu, J.M. Cowley, Ultramicroscopy **53**, 333 (1994).
26. A.A. Lucas, V. Bruyninckx, Ph. Lambin, Europhys. Lett. **35**, 355 (1996).
27. D. Bernaerts, Ph.D thesis, University of Antwerpen, 1997.
28. J.M. Cowley *et al.*, Chem. Phys. Lett. **265**, 279 (1997).
29. L.C. Qin *et al.*, Chem. Phys. Lett. **268**, 101 (1997).
30. D. Bernaerts *et al.*, Solid State Commun. **105**, 149 (1998).
31. Ph. Lambin, A.A. Lucas, Phys. Rev. B **56**, 3571 (1997).
32. M. Tachibana, K.A. Williams, S.L. Fang, E. Richter, P.C. Eklund (to be published in the Proceedings of the International Workshop on the Science and Applications of Nanotubes, East Lansing, USA, July 1999).
33. M. Knupfer, T. Pichler, M.S. Golden, J. Fink, A. Rinzler, R.E. Smalley, Carbon **37**, 733 (1999).